Electric Power Systems Research 140 (2016) 643–652

Contents lists available at ScienceDirect

Electric Power Systems Research

journal homepage: www.elsevier.com/locate/epsr

Multi-parameter bifurcation analysis of subsynchronous interactions in DFIG-based wind farms

Gustavo Revel[a,b,*], Andres E. Leon[a], Diego M. Alonso[a,b], Jorge L. Moiola[a,b]

[a] Instituto de Investigaciones en Ing. Eléctrica (IIIE) Alfredo Desages (UNS-CONICET), Argentina
[b] Depto. de Ing. Eléctrica y de Computadoras, Universidad Nacional del Sur, Av. Alem 1253, (8000) Bahía Blanca, Argentina

ARTICLE INFO

Article history:
Received 26 August 2015
Received in revised form 31 March 2016
Accepted 8 May 2016
Available online 14 June 2016

Keywords:
Power system dynamics
Subsynchronous interaction
Doubly-fed induction generator
Bifurcation analysis

ABSTRACT

This work analyzes the dynamics involved in subsynchronous interactions between wind farms and series-compensated transmission lines. This adverse phenomenon may arise when doubly-fed induction generators are radially connected to an ac transmission line with series capacitive compensation. The resulting subsynchronous oscillations can produce the system instability and cause a severe damage to the wind turbines. The study is carried out combining tools from bifurcation theory, eigenvalue analysis and nonlinear time-domain simulations. The impact on the subsynchronous mode due to the variation of a set of key parameters is considered. These parameters include the series compensation of the transmission line, the wind speed (generated power), the wind energy penetration level, and a gain of the internal control loop of the wind turbine. The bifurcation study determines that the underlying mechanism associated with the appearance of subsynchronous oscillations can be explained by means of Hopf bifurcations of the equilibrium point and their corresponding limit cycles. In addition, the saturation of the wind turbine converters plays an important role in the dynamics, introducing non-smooth bifurcations that are also analyzed.

1. Introduction

The location of large wind farms (WFs) is mainly determined by the availability of the wind resource. In many cases the optimal regions are distant from the load centers, and long ac transmission lines are necessary to deliver the wind power. In order to maximize the power flow over these long lines (typically more than 200 km [1]) the inductive reactance is often compensated using series capacitors. This is a cost effective way of improving power transfer increasing the transient and voltage stability limits, and reducing losses by sharing the power flow between parallel lines [2]. It is well known that this kind of compensation can introduce the risk of subsynchronous interactions (SSI) in which two or more parts of the electrical system exchange energy at one or more of the natural frequencies of the combined system below the nominal frequency [3,4]. In general, the SSI phenomenon is classified into three main categories: (i) sub-synchronous resonance (SSR), when a series compensated line interacts with a turbine-generator; (ii) sub-synchronous torsional interaction (SSTI), when a turbine-generator interacts with a power electronic controller; and (iii) sub-synchronous control interaction (SSCI), when a series compensated line interacts with a power electronic device (see [4–6]). In addition, the SSR category can be divided into mechanical and electrical events as: (a) torsional interaction (TI) and torque amplification (TA), when the line interacts (in steady state or transiently, respectively) with the mechanical part of the turbine-generator, and (b) induction generator effect (IGE) when the line interacts with the electrical part of the generator. Notice that mechanical SSR (TI and TA) and SSTI involve fixed mechanical torsional modes of the turbine-generator, whereas the resonance frequency concerned with IGE depends on the electrical parameters of the generator and the grid. It is worth to mention that the frequency of SSCI depends not only on the grid parameters but also on the control tuning, and since the turbine-generator mechanical parts are not involved, the resulting oscillations can grow faster than those arising in mechanical SSR [4].

Subsynchronous interactions in WFs based on doubly-fed induction generators (DFIG), received special attention in the last few years. The most significant incident occurred in 2009 in Texas, where after a contingency, two WFs became radially connected to a series-compensated line (the nominal compensation was 50%, but

* Corresponding author at: Depto. de Ing. Eléctrica y de Computadoras, Universidad Nacional del Sur, Av. Alem 1253, (8000) Bahía Blanca, Argentina.
Tel.: +54 02914595180.
E-mail addresses: grevel@uns.edu.ar (G. Revel), aleon@iiie-conicet.gob.ar (A.E. Leon), dalonso@uns.edu.ar (D.M. Alonso), jmoiola@uns.edu.ar (J.L. Moiola).

http://dx.doi.org/10.1016/j.epsr.2016.05.009
0378-7796/

after a change of the grid topology it was above 75%). The event triggered subsynchronous oscillations (SSO) due to the interaction of the series capacitors of the transmission line and the current control loop of the DFIG, causing severe damages not only to the capacitor bank but also to the wind power converters. It was concluded that SSO were caused mainly by the rotor current control loop of the DFIG, and it was classified as a SSCI phenomenon [3,4,7]. A modal analysis performed in [6] reveals that increasing the gain of that control loop shifts the subsynchronous mode towards the right-half-plane (reducing its damping). In addition, the mechanical modes of the wind turbine are not affected by parameter variations (TI and SSTI do not appear). This incident captured the attention of power system operators and researchers. The effect of different parameters and operating conditions on the main modes of interest (sub and supersynchronous, electromechanical and torsional modes) were investigated in [8,9] using small signal and modal analyses, and time domain simulations. The problem was also analyzed using the Nyquist criterion on a derived impedance model in [10]. A procedure to study SSI in wind farms was presented in [11] and a general methodology was proposed in [12]. Mitigation strategies using dedicated controllers were analyzed in [6,13–18], and using Flexible AC Transmission Systems (FACTS) in [19–21]. SSO also appeared in a 150 MVA DFIG wind farm located in Minnesota, USA. In this case, the triggering condition was similar to the one experienced in Texas, i.e., after a fault on the system the wind farm became radially connected with a corridor with 60% of series compensation [22]. Another incident was reported in the north of China, where a 3000 MVA wind generation (composed mostly of DFIG turbines) experienced very low-frequency oscillations [23,24]. The problem was associated to SSI and in this case, the oscillations vanished after the successive disconnection of generation units.

In this work, the SSI in DFIG-based WFs are analyzed using tools from nonlinear dynamics theory aiming to complement the previous analytical and numerical studies. Nonlinear analysis techniques, including bifurcation theory, offer powerful methods to study problems characterized by the appearance of nonlinear oscillations when certain parameters are varied. They have been successfully used to study the dynamical behavior of power systems in diverse contexts, such as stability analysis [25–30], integration of wind energy [31,32], and the SSR phenomenon in conventional synchronous generators [33,34]. In this study, bifurcation theory is used in combination with classical methods, such as, eigenvalue analysis and nonlinear time-domain simulations. A power system consisting of a DFIG-based WF exporting energy through a series-compensated corridor is considered. The impact on the system dynamics due to changes in different key parameters such as the series compensation level, the wind speed, the gain of the rotor current controller and the WF rated power (penetration level) is investigated. Towards this end, the mechanisms (bifurcations) leading to SSCI, are analyzed using one-, two- and three-parameter bifurcation diagrams. The main contribution consists in providing a detailed description about the influence of the bifurcation parameters on the SSCI phenomenon, revealing the mechanisms responsible for the loss of the local stability of the operating point (equilibrium). The amplitude and stability of the emerging periodic oscillations (limit cycles) are also computed. Since the control scheme of the wind turbine includes saturation limits, non-smooth bifurcations of limit cycles are also analyzed.

The paper is organized as follows. In Section 2, we describe the model and we define the dynamics in the context of piecewise-smooth systems. The nonlinear dynamical analysis varying one parameter at a time is performed in Section 3, and in Section 4 two- and three-parameter bifurcation diagrams are developed. Finally, Section 5 presents the conclusions of the analysis.

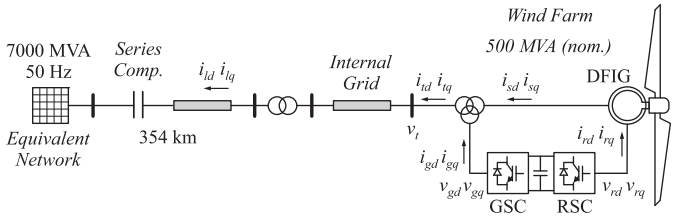

Fig. 1. Single-line representation of the power system considered.

2. Power system model for SSCI studies

The power system considered in this study (see Fig. 1) consists in a DFIG-based WF connected to a 7000 MVA/50 Hz equivalent network via a series-compensated transmission line of 500 kV and 354 km long. The nominal generation capacity of the WF is 500 MVA, although different values of the rated apparent power will be considered in order to investigate the impact of the penetration level on the SSCI phenomenon. The line parameters correspond to a portion of the Patagonia corridor of the Argentine interconnected system. The Patagonia region (south of Argentina) is very attractive for the development of wind energy projects (due to high power densities and capacity factors), hence a large quantity of wind generation is expected to be added in the near future. Since, practically all the wind energy generated will be exported to the bulk load centers using this radial corridor, the transmission system operator is planning to enhance the transport capabilities not only by including new parallel lines, but also using fixed series compensation.[1] In this study, the first part of the corridor (354 km, between the cities of Choele-Choel and Puerto Madryn) is considered (see a diagram of the system in [18]). It is assumed that the power demand on this corridor is satisfied by internal conventional generation, and all the power generated by the WF is delivered to the interconnected power system (equivalent network) through a series compensated line. Thus, the attention is focused on the SSI problem in order to perform a detailed non-linear analysis using bifurcation tools. This enables a direct interpretation of the associated dynamics as well as the extension of the results to more general cases. The multi-parameter bifurcation analysis, is useful in the determination of feasible operating regions, as well as in the identification of non-feasible regions where equilibria and sustained oscillations coexist due to smooth and non-smooth (saturations) nonlinearities. A brief description of the models used in this study with a complete list of system parameters and typical power flows are given in Appendix A.

2.1. Wind farm model

The WF is represented by an aggregated model of DFIG wind turbines. The mechanical part of the generator is modeled using a six-mass system, while the turbine characteristic is approximated using the power curve given in [35]. A classical vector control scheme in *d-q* coordinates for DFIG machines is implemented (see details in [36,37]). The electrical variables of the wind turbine are shown in Fig. 1.

The control scheme of the RSC is shown in Fig. 2(a). The blue rectangle denotes the vector control in *d–q* coordinates consisting in two internal proportional-integral (PI) loops, and two external PI loops with smaller bandwidth.[2] The internal loops control the

[1] Preliminary studies suggest that the series compensation of some important lines in the Patagonia corridor will be around 70%.

[2] The PI controllers have anti-windup action based on the back-calculation method [38].

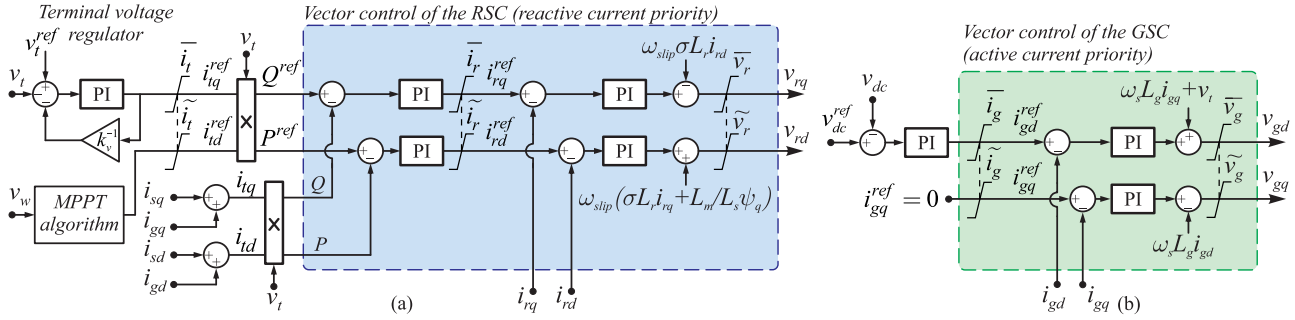

Fig. 2. Vector control of the power converters of the DFIG. (a) RSC. (b) GSC. PI controllers are implemented in the standard form, i.e., $PI(s) = K[1 + (T_i s)^{-1}]$. The limits for the components with priority are constant and indicated with (—), while the limits for the ones without priority are variable and denoted with (∼). (For interpretation of the references to color in text near the reference citation, the reader is referred to the web version of this article.)

rotor currents i_{rd} and i_{rq}, by adjusting the RSC voltages v_{rd} and v_{rq}, respectively. Their references i_{rd}^{ref} and i_{rq}^{ref} are computed by the external loops. The d-axis outer loop controls the total active power P injected by the DFIG according to the reference P^{ref}, obtained from a maximum power point tracker (MPPT) algorithm. The q-axis loop controls the total reactive power Q according to the reference Q^{ref}, obtained from an external voltage regulator [PI with droop $K_v^{-1} = 5\%$, in Fig. 2(a)]. Notice that in this simplified system the equivalent WF performs voltage regulation on the connection node.

The control of the GSC is represented in Fig. 2(b). The vector control (green rectangle) is achieved by two PI current loops, regulating the converter voltages v_{gd} and v_{gq}. The d-axis current i_{gd} is used to maintain the voltage of the dc-link at the reference value v_{dc}^{ref} with a PI controller. The q-axis current i_{gq} can be used to inject reactive power to the grid, but in this case the reference is set to zero ($i_{gq}^{ref} = 0$).

2.2. Limitation of the DFIG control signals

The reference signals of the DFIG vector control and the voltages of the converters are limited using a priority scheme [39]. The RSC prioritizes the reactive power injection (q-axis), since it is required to maintain the terminal voltage in case of a fault near the WF (satisfying the grid code regulations). Therefore the components with priority for the RSC are i_{tq}^{ref}, i_{rq}^{ref} and v_{rq}, with fixed limits given by the maximum moduli of the total current ($\bar{i}_t$), the rotor current ($\bar{i}_r$) and the rotor voltage ($\bar{v}_r$), respectively [see Fig. 2(a)]. The limits of the d-axis non-priority components i_{td}^{ref}, i_{rd}^{ref} and v_{rd}, denoted $\widetilde{i}_t$, $\widetilde{i}_r$ and $\widetilde{v}_r$, respectively, are adjusted according to the corresponding q-axis components. On the other hand, the GSC prioritizes the active power injection (d-axis), since its main goal is to regulate the voltage of the dc-link. In this case, the components with priority are i_{gd}^{ref} and v_{gd}, with maximum moduli $\bar{i}_g$ and $\bar{v}_g$, respectively. The ones without priority are i_{gq}^{ref} and v_{gq}, with variable limits $\widetilde{i}_g$ and $\widetilde{v}_g$, respectively. Notice that the limits are imposed to the internal variables of the controllers and not directly to the states (e.g., the reference i_{gd}^{ref} is limited but not the state i_{gd}).

Suppose a generic internal variable $\eta \in R^2$ with components η_1 and η_2, and that the priority is assigned to η_1. If the modulus of η must be limited to $\bar{\eta}$ (i.e., a circle of radius $\bar{\eta}$ in the plane $\eta_1 - \eta_2$), the priority scheme imposes that η_1 has to be limited to $\pm\bar{\eta}$ (fixed) and η_2 to $\pm\widetilde{\eta}$ (variable), where $\widetilde{\eta} = \sqrt{\max(\bar{\eta}^2 - \eta_1^2, 0)}$. These limits can be written as the zero sets of the real valued functions $H_1(\eta) = \bar{\eta} - |\eta_1|$ and $H_2(\eta) = \bar{\eta}^2 - (\eta_1^2 + \eta_2^2)$, defining in the plane $\eta_1 - \eta_2$ five regions S_i, $i = 1, \ldots, 5$ as depicted in Fig. 3. The borders between the regions are defined by the non-empty intersections of the closure of the sets S_i, i.e., $\Sigma_{ij} = \bar{S}_i \cap \bar{S}_j$. On each region S_i, the dynamics is represented by (different) smooth dynamical systems, and the borders Σ_{ij} are referred to as discontinuity (switching) boundaries. This setting defines a piecewise smooth (PWS) system: $\dot{x} = F_i(x, \eta; \lambda)$ for $\eta \in S_i$ $(i = 1, \ldots, 5)$, where F_i are sufficiently smooth functions in a domain $D \subset R^n$. Thus, in S_1 (light blue region in Fig. 3) none of the components are restricted, and the corresponding smooth function is $F_1 = F$ (i.e., the model of the system without restrictions). But, for example, crossing Σ_{12} from S_1 to S_2 (upper green region), the component without priority η_2 becomes limited to $\widetilde{\eta} = \sqrt{\bar{\eta}^2 - \eta_1^2}$, resulting in the system F_2 (i.e., F with $\eta_2 = \widetilde{\eta}$). When Σ_{14} is crossed from S_1 to S_4 (yellow region to the right), the prioritized component η_1 is limited to $\eta_1 = \bar{\eta}$ and $\eta_2 = 0$, defining the system F_4.

The vector control of the DFIG converters has limits on five internal signals, and the corresponding restrictions define two functions $H_{1,k}$ and $H_{2,k}$ $(k = 1, \ldots, 5)$, and five regions $S_{i,k}$ for each signal. Therefore, the complete PWS system is obtained by combining these conditions and defining the associated smooth functions F_i with the corresponding restrictions on the five signals with limits. Notice that the non-smooth phenomena analyzed in this paper involve crossing of a single boundary at a time.

3. Nonlinear analysis of SSCI

Subsynchronous control interaction between DFIG-based wind farms and series compensated transmission lines is an entirely electrical phenomenon, with non-fixed frequency [4]. The bandwidth of the DFIG control loops plays a relevant role in this phenomenon, and is revealed by varying the gain K of the rotor current PI controllers (denoted K_{ir}). The SSCI is also affected by the compensation

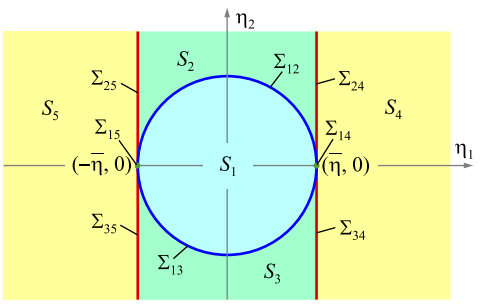

Fig. 3. Regions S_i and discontinuity boundaries Σ_{ij} of the generic limitation scheme. (For interpretation of the references to color in text near the reference citation, the reader is referred to the web version of this article.)

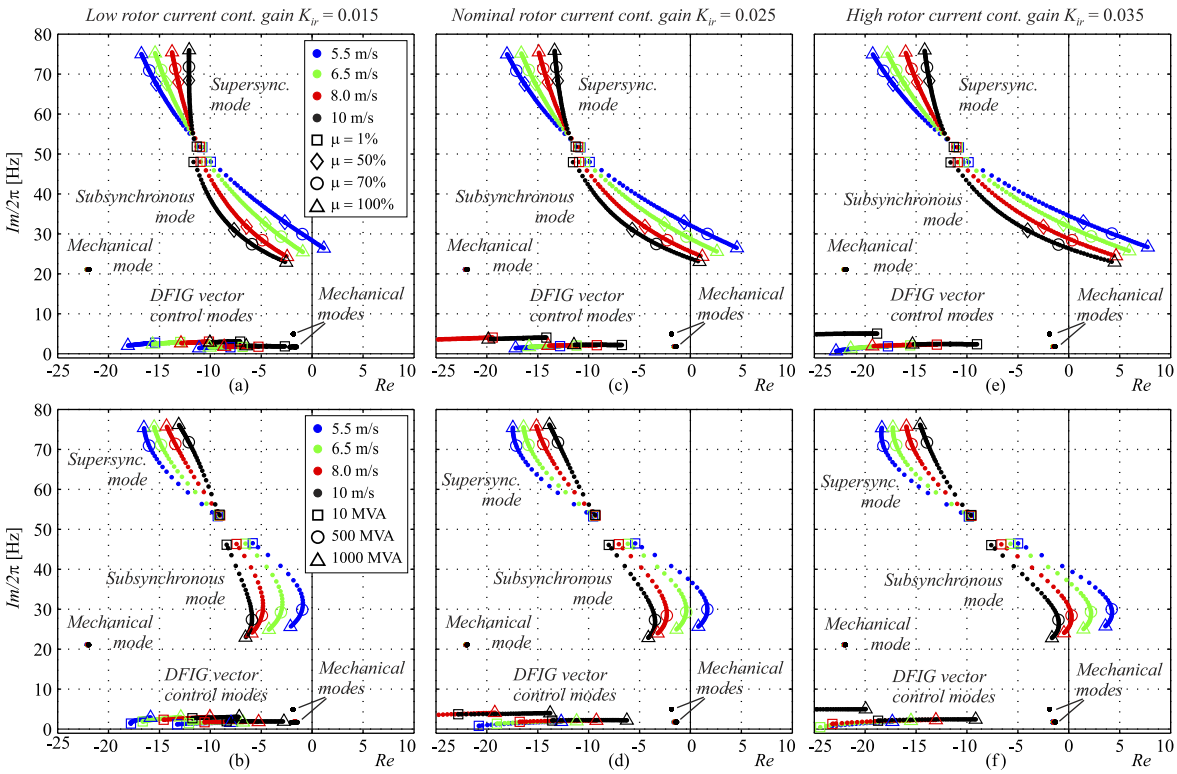

Fig. 4. Loci of the relevant eigenvalues. (a), (c) and (e) are obtained varying μ for $v_w = \{5.5, 6.5, 8, 10\}$ m/s and $S_B = 500$ MVA. (b), (d) and (f) are obtained varying S_B for the same wind speeds and $\mu = 70\%$. The columns denote three gain values of the rotor current control loop: $K_{ir} = \{0.015, 0.025, 0.035\}$.

level[3] (μ), the wind speed (v_w) and the rated power of the WF (S_B). In this section, the dynamics is analyzed in terms of these parameters, varying one of them at a time, using the software package Matcont [40]. The software is robust and accurate in detecting smooth bifurcations in ordinary differential equations and computes the normal form coefficients of codimension-one and -two bifurcations of equilibrium points and limit cycles. It is also robust in continuing limit cycles even in the presence of non-smooth restrictions. The detection of non-smooth bifurcations is carried out by checking the functions $H_{1,k}$ and $H_{2,k}$ for each solution obtained from the continuation, capturing the value of the parameter when a boundary is reached. The maximum continuation step is adjusted in order to determine the non-smooth phenomena with a good accuracy.

3.1. Loci of the relevant eigenvalues

The loci of the most relevant eigenvalues of the system under study are shown in Fig. 4, where three different values of the rotor current controller gain K_{ir} are considered. Let us describe in detail the case with nominal gain $K_{ir} = 0.025$, shown in the second column. The cases with $K_{ir} = 0.015$ and $K_{ir} = 0.035$ are shown in the first and third columns, respectively.

Fig. 4(c) depicts the eigenloci varying the compensation level μ, with the rated power of the wind farm fixed at $S_B = 500$ MVA and four different wind speeds. When the compensation is very low, the subsynchronous mode has an acceptable damping for all wind conditions (see the eigenvalues for $\mu = 1\%$, denoted by squares). When μ is increased, this mode moves towards the right-half plane, decreasing the frequency and damping. It becomes unstable (e.g., $\mu > 55\%$ for $v_w = 5.5$ m/s, or $\mu > 94\%$ for $v_w = 10$ m/s) due to a Hopf bifurcation. On the other hand, the supersynchronous mode moves towards the left and the frequency increases. Therefore, there is a small reduction of the damping factor, but less considerable than the one suffered by the subsynchronous mode. Fig. 4(c) also shows the effect of the wind speed variation. For example, for a fixed compensation $\mu = 70\%$ (empty circle markers in the figure), the damping of the subsynchronous mode is reduced when the wind speeds decreases (and becomes unstable for $v_w < 6.5$ m/s). The same behavior is observed for other values of μ and K_{ir}. Thus, for low wind conditions, the system is more susceptible to undergo SSCI.

Fig. 4(d) depicts the eigenvalues varying the WF rated power (S_B), with the compensation fixed at $\mu = 70\%$ and different wind speeds (the same colors are used to denote the previous wind conditions). The behavior of the subsynchronous mode is slightly different from the one observed varying μ. Initially, the increase of S_B moves the subsynchronous mode towards the right, reducing the damping and frequency [and in some cases it becomes unstable, as shown in Fig. 4(d) and (f)]. This continues until the real part finds a maximum value (for $S_B \simeq 500$ MVA), and then the mode turns back towards the left. The movement of the supersynchronous mode is similar to the one observed varying μ.

Notice that regardless which parameter is varied (μ or S_B), the mechanical modes (with frequencies around 2, 6 and 20 Hz) are practically unperturbed. Therefore, in this case there are no torsional interactions between the grid and the mechanical modes of the wind turbine (also observed in [17]).

3.2. One-parameter bifurcation analysis varying μ

As mentioned in Section 3.1, the system may become unstable due to a Hopf bifurcation. The associated dynamics is studied performing a one parameter bifurcation analysis for the same scenario of Fig. 4(c), i.e., $S_B = 500$ MVA, nominal gain $K_{ir} = 0.025$,

[3] The compensation level is defined as the ratio between the reactance of the compensation capacitor (X_C) and the reactance of the transmission line (X_L), i.e., $\mu = X_C/X_L$.

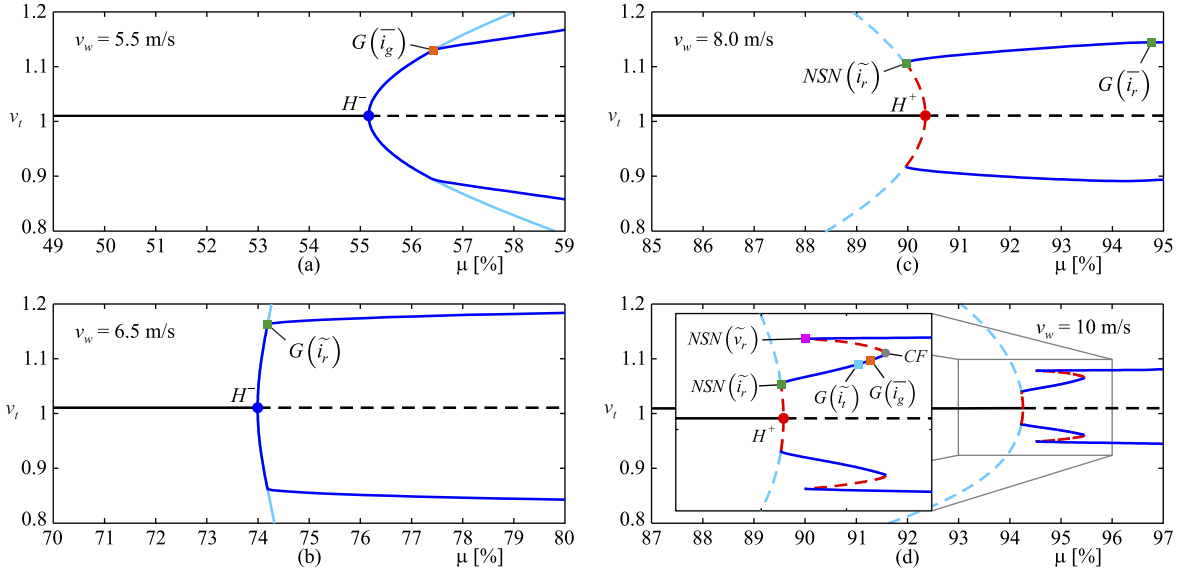

Fig. 5. Bifurcation diagrams varying μ, with $K_{ir} = 0.025$ (nominal) and $S_B = 500$ MVA.The Hopf bifurcations (denoted $H^{\pm}$) correspond to the crossing of the subsynchronous mode depicted in Fig. 4(c). (a) $v_w = 5.5$ m/s. (b) $v_w = 6.5$ m/s. (c) $v_w = 8.0$ m/s. (d) $v_w = 10$ m/s. (For interpretation of the references to color in text near the reference citation, the reader is referred to the web version of this article.)

and four different wind speeds. The corresponding bifurcation diagrams are shown in Fig. 5, with the parameter μ in the abscissa and the terminal voltage (v_t) in the ordinate. The equilibrium point is denoted in black, and colors are used to represent the amplitude of the limit cycles. In both cases, solid curves represent stable solutions and dashed curves unstable ones.

Let us begin the description with the bifurcation diagram for $v_w = 5.5$ m/s, shown in Fig. 5(a). In this case, the equilibrium point becomes unstable for $\mu \simeq 55.2\%$ due to a supercritical Hopf bifurcation (H^-) when the subsynchronous mode crosses the imaginary axis [see Fig. 4(c)], and a stable limit cycle emerges[4] for increasing values of μ. The amplitude grows until the reference current of the GSC reaches the maximum value ($\bar{i}_g$) for $\mu \simeq 56.4\%$. At this point, denoted by $G(\bar{i}_g)$ (orange square), the system grazes the discontinuity boundary associated to the component with priority i_{gd}^{ref} (in the generic scheme of Fig. 3, the boundary is Σ_{14} dividing S_1 and S_4), and undergoes a non-smooth grazing bifurcation [42,43]. In this case, the grazing bifurcation does not change the stability of the limit cycle but it modifies the amplitude of the oscillation, as can be observed when comparing with the one obtained by removing the limiter block (cyan curve).

Fig. 5(b) shows the bifurcation diagram for $v_w = 6.5$ m/s. This case is similar to the one shown in Fig. 5(a), but the grazing bifurcation (green square marker) is due to the saturation of the reference current of the RSC. The point is labeled $G(\tilde{i}_r)$, since it corresponds to the component without priority i_{rd}^{ref}. The amplitude of the oscillation on the terminal voltage v_t is larger than the case with $v_w = 5.5$ m/s. This phenomenon can be explained by the proximity of a codimension-two singularity given by a degeneration of the Hopf bifurcation, that will be explained in Section 4.1.

The bifurcation diagram for $v_w = 8.0$ m/s is shown in Fig. 5(c). The Hopf bifurcation is now subcritical (H^+) and an unstable limit cycle is created for decreasing values of μ (dashed red curve). This unstable limit cycle grazes a switching boundary when i_{rd}^{ref} (non-prioritized) reaches the saturation value for $\mu \simeq 90\%$, at the point labeled $NSN(\tilde{i}_r)$ (green square marker). The scenario is very different from the previous cases, since now a stable oscillation (not present in the system without saturations) is introduced by a non-smooth saddle-node bifurcation $NSN(\tilde{i}_r)$. The mechanism associated to this change in the dynamics is a codimension-two singularity (of limit cycles) that it will be explained later by means of a two-parameter bifurcation analysis. For increasing values of μ, the stable limit cycle evolves towards the right and suffers a second grazing bifurcation $G(\bar{i}_r)$, when the component with priority i_{rq}^{ref} saturates.

The bifurcation diagram for $v_w = 10$ m/s is shown in Fig. 5(d). For this wind speed, the generator operates close to the maximum ratings, and multiple grazing bifurcations are expected to occur when oscillations arise. As depicted in the blow-up, the Hopf bifurcation is subcritical (H^+) and an unstable limit cycle emerges. Almost immediately the cycle undergoes a non-smooth saddle-node bifurcation $NSN(\tilde{i}_r)$ (green square marker) when the rotor current reference i_{rd}^{ref} reaches the limit. Then, the stable limit cycle exhibits two consecutive grazing bifurcations without changing the stability of the cycle. The first one $G(\tilde{i}_t)$ (cyan marker), due to the saturation of the total active current of the machine i_{td}^{ref}, and the second $G(\bar{i}_g)$ (orange marker) due to the active current of the GSC i_{gd}^{ref}. After the grazing bifurcations, the stable cycle collapses in a smooth saddle-node of limit cycles CF (gray marker) and an unstable cycle emerges towards the left. This cycle suffers a non-smooth saddle-node $NSN(\tilde{v}_r)$ (pink square marker) given by the saturation of the d-axis voltage of the RSC v_{rd}, and a stable limit cycle emerges for increasing values of μ. A similar structure of limit cycles was observed in [42], induced by the limits of the AVR/PSS of a synchronous generator.

3.3. Time-domain simulations of switching limit cycles

In order to illustrate the effect of the grazing bifurcations on the limit cycles, distinctive time-domain simulations[5] are performed. Each column in Fig. 6 shows one period of a stable limit cycle for three different wind speeds (5.5, 6.5 and 8.0 m/s). In all cases,

[4] The superscript ($\pm$) on the Hopf bifurcation denotes the sign of the first Lyapunov index, and defines the stability of the emerging limit cycle: stable when it is negative (supercritical), and unstable when it is positive (subcritical) [41].

[5] The simulations results were obtained with Matlab®.

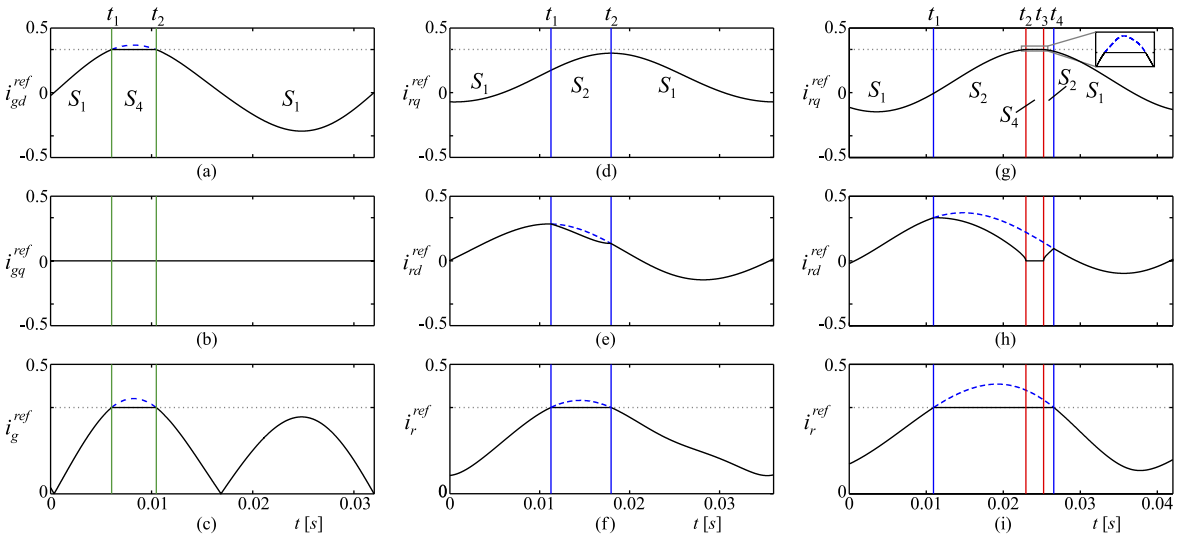

Fig. 6. Reference signals involved in the grazing bifurcations of Fig. 5(a)–(c). Panels (a)–(c) correspond to $v_w = 5.5$ m/s and $\mu = 58\%$; (d)–(f) to $v_w = 6.5$ m/s and $\mu = 78\%$; and (g)–(i) to $v_w = 8.0$ m/s and $\mu = 95\%$.

the desired values for the references are depicted by dashed blue lines, the transitions through the switching boundaries are denoted by vertical lines, and the dotted gray horizontal lines indicate the maximum value allowed for the component with priority and the modulus of the corresponding signal. Since the size of the power converters of the DFIG is one-third of the turbine rated power, the maximum moduli of the reference currents of the converters are limited to 1/3 [pu].

From the bifurcation diagram of Fig. 5(a), for $\mu = 56.4\%$ the system undergoes a non-smooth grazing bifurcation $G(\bar{i_g})$ when the component with priority i_{gd}^{ref} reaches the limit. Hence, for $\mu = 58\%$ the cycle exhibits the effect of this bifurcation, as denoted in the first column of Fig. 6. This is a particular case, since the reactive current of the GSC is zero, i.e., $i_{gq}^{ref} = 0$. Thus the limit $\widetilde{i_g}$ does not affect the dynamics and the priority scheme reduces to a conventional saturation [see Fig. 6(a)]. According to the generic interpretation given in Fig. 3, for $0 < t < t_1$, no restrictions are applied and $\|\eta\| < \bar{\eta}$ [see Fig. 6(c)], the system is in region S_1 and evolves on the horizontal axis. When $t = t_1$, i_{gd}^{ref} reaches the limit $\bar{i_g}$, the system crosses the discontinuity boundary Σ_{14} from S_1 to S_4, where i_{gd}^{ref} is limited. When $t = t_2$, the system crosses again the boundary Σ_{14} back to S_1. Notice that the grazing bifurcation occurs when $t_1 = t_2$, for $\mu \simeq 56.4\%$.

The second column of Fig. 6 shows one period of the stable limit cycle for $v_w = 6.5$ m/s and $\mu = 78\%$. In this case, the component involved in the grazing bifurcation [denoted $G(\widetilde{i_r})$ for $\mu \simeq 74.2\%$ in Fig. 5(b)] is the rotor active current i_{rd}^{ref}. This scenario is different from the one described above (first column), since the component with priority, i_{rq}^{ref}, never exceeds the limit $\bar{i_r}$ [cf. Fig. 6(a) and (d)]. On the other hand, the component without priority i_{rd}^{ref}, is limited for $t_1 < t < t_2$. Recalling Fig. 3, at $t = t_1$, the system crosses the discontinuity boundary Σ_{12}, from region S_1 to S_2, and it returns to S_1 at $t = t_2$.

The third column of Fig. 6 shows a stable limit cycle for $v_w = 8.0$ m/s and $\mu = 95\%$. At this compensation level the limit cycle emerged at H^+ has suffered two grazing bifurcations, due to the limitation of the rotor current. The first one (for $\mu \simeq 90\%$) corresponds to the component without priority i_{rd}^{ref}, and the second (for $\mu \simeq 94.8\%$) to the component with priority i_{rq}^{ref}. Thus the effect is observed on both components as shown in Fig. 6(g) and (h). According to the diagram of Fig. 3, for $0 < t < t_1$, the system is in region S_1, i.e., without restrictions. At $t = t_1$, the modulus of the signal reaches the limit and the component without priority i_{rd}^{ref} becomes limited, entering region S_2. At $t = t_2$, the system crosses from region S_2 to S_4, where $i_{rd}^{ref} = 0$ and the component with priority i_{rq}^{ref} is limited. Then it returns to S_2 at $t = t_3$ and to S_1 at $t = t_4$. Notice that when $\mu \simeq 94.8\%$ [bifurcation $G(\bar{i_r})$ in Fig. 5(c)], the cycle grazes the boundary Σ_{24} and $t_2 = t_3$. On the other hand at the non-smooth saddle-node point $NSN(\widetilde{i_r})$ for $\mu \simeq 90\%$, the cycle grazes the boundary Σ_{12} and $t_1 = t_4$.

The case of Fig. 5(d), for $v_w = 10$ m/s, involves multiple grazing points as μ is varied following the limit cycle. Nevertheless, the behavior of the limited signals is similar to those explained above.

4. Two- and three-parameter bifurcation analyses

The analysis in Section 3 shows the general behavior of the modes and the bifurcations associated to the SSI phenomenon, when one parameter varies and the others are left fixed. Based on these results, it is not trivial to determine how the modes and bifurcation conditions change when arbitrary values of the parameters are selected. In this regard, a multi-parameter bifurcation analysis clue us in how the dynamics related to SSI is organized, determining the distance to the instability (Hopf or limit cycle bifurcations) for a given set of parameters and at the same time explaining the changes in the dynamics observed in the different cases studied in Section 3.2.

The bifurcation parameters used for the multi-parameter analysis coincide with the ones considered in Section 3, i.e., μ, v_w, S_B and K_{ir}. In order to describe the dynamics on a broad set of conditions, the compensation level is varied within the maximum theoretical range 0–100%,[6] and the WF rated power within 0–1000 MVA (which is approximately the maximum power admissible by the line considered in this study). In addition, the wind speed varies along the MPPT curve, and three values of K_{ir} are used. It is important to notice that, although some of the phenomena may be observed at values near the theoretical limits (for a given set of parameters), they can be displaced affecting feasible operating regions, when other key parameters are varied. A clear example

[6] Although a 100% compensation level is not reached in practice, a high value may result after a contingency and the subsequent grid reconfiguration as in the ERCOT case. In addition, in our case μ only considers the inductance of the high voltage transmission line and excludes the rest of the inductances such as the one from the WF internal grid.

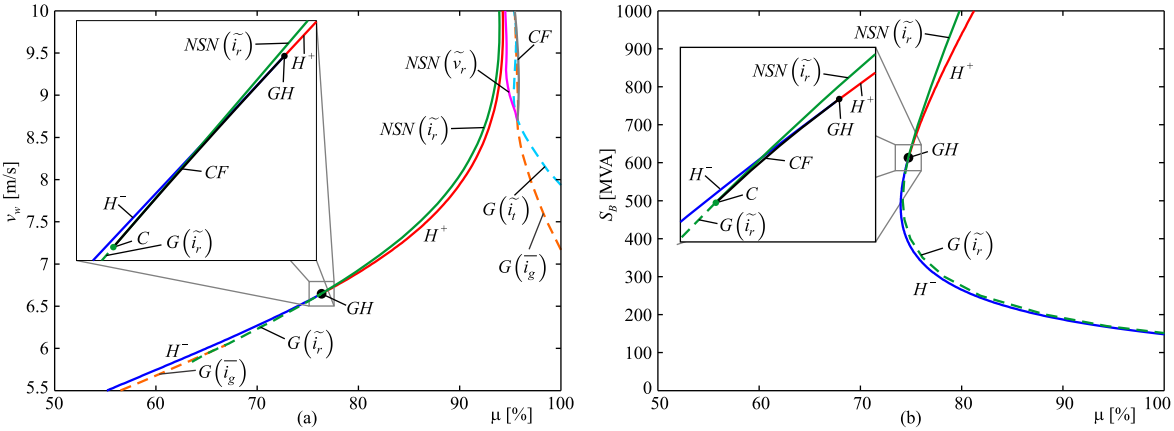

Fig. 7. Two-parameter bifurcation diagrams. (a) Varying μ and v_w with $K_{ir} = 0.025$ and $S_B = 500$ MVA. (b) Varying μ and S_B with $K_{ir} = 0.025$ and $v_w = 6.5$ m/s. (For interpretation of the references to color in text near the reference citation, the reader is referred to the web version of this article.)

of such behavior will be presented at the end of this section, when the effect of the rotor current control gain K_{ir} is analyzed.

4.1. Two-parameter analysis

The one-parameter bifurcation analysis shows that sustained oscillations developed in SSCI arise in a Hopf bifurcation of the equilibrium point, followed by grazing bifurcations of the emerging limit cycle due to saturations. One of the most relevant aspects is the transition from the bifurcation diagram of Fig. 5(b), where the limit cycle is stable and the grazing bifurcation does not change the stability of the cycle, to the one shown in Fig. 5(c), where the emerging limit cycle is unstable and the grazing produces a non-smooth saddle-node bifurcation of limit cycles (generating a stable oscillation). The transition can be explained by performing a two-parameter bifurcation analysis. First we deal with the same parameters involved in Fig. 5, i.e., μ and v_w, using $S_B = 500$ MVA as the rated power of the WF. Then, we consider simultaneous variations of μ and S_B, for $v_w = 6.5$ m/s. In both cases, the nominal gain for the rotor control loop ($K_{ir} = 0.025$) is used.

The two-parameter curves corresponding to non-smooth bifurcations are obtained performing repeated one-parameter continuations for consecutive fixed values of the second parameter. Then, the points are joined together according to the type of bifurcation and the internal variable that reaches the limit. The rest of the curves (smooth bifurcations) are obtained by direct continuation of the corresponding singularity varying two parameters simultaneously.

4.1.1. Bifurcation diagram varying μ and v_w

The diagram is shown in Fig. 7(a), where the abscissa is the compensation level μ and the ordinate is the wind speed v_w. The Hopf bifurcation curve of the equilibrium point is denoted in blue (H^-) and red (H^+), to indicate when it is supercritical and subcritical, respectively. This curve divides the parameter space into a stable operation region to the left and an unstable one to the right. Thus, the lower the wind speed, the lower the compensation level where the equilibrium point becomes unstable (triggering an SSCI). The remaining curves correspond to limit cycle bifurcations. The dashed curves are grazing bifurcations (G) and the solid curves denote non-smooth saddle-node bifurcation of limit cycles (NSN).[7] The solid black curve is a smooth saddle-node bifurcation of limit cycles or cyclic fold (CF).

The Hopf bifurcation curve changes from supercritical (H^-) to subcritical (H^+) at $(\mu, v_w) \simeq (76.33, 6.65)$, where the first Lyapunov index of the Hopf bifurcation becomes zero [black dot in Fig. 7(a)]. This codimension-two singularity is known as generalized Hopf bifurcation (GH), and it unfolds a curve of saddle-node bifurcations of limit cycles [41]. This curve, denoted CF in the blow-up of Fig. 7(a), interacts with the grazing bifurcation curve $G(\widetilde{i_r})$, at the point C. This is a second codimension-two singularity, but now involving limit cycles. At this point, the grazing bifurcation curve $G(\widetilde{i_r})$, which does not modify the stability of the limit cycle, changes qualitatively to the non-smooth saddle-node bifurcation curve $NSN(\widetilde{i_r})$ which destroys the unstable cycle and introduces a stable one [c.f. Fig. 5(b) and (c)]. A similar structure was studied in [44] regarding a buck converter. The schematic representation of the interacting bifurcation curves is shown in Fig. 8(a), and the phase diagrams corresponding to each region are depicted in Fig. 8(b)–(f). In these diagrams the abscissa is the total active current (i_{td}) and the ordinate is the terminal voltage (v_t). The stable equilibrium points are represented by black dots (empty when they are unstable), the stable limit cycles with solid blue curves and the unstable cycles are with dashed red lines. In region 1, there is only a stable equilibrium point [Fig. 8(b)]. This equilibrium becomes unstable and a stable limit cycle is created when the supercritical Hopf curve H^- is crossed in the transition from region 1 to region 2 [Fig. 8(c)]. The stable limit cycle of region 2 suffers a grazing bifurcation when the curve $G(\widetilde{i_r})$ is crossed to get into region 3 [Fig. 8(d)]. The crosses in

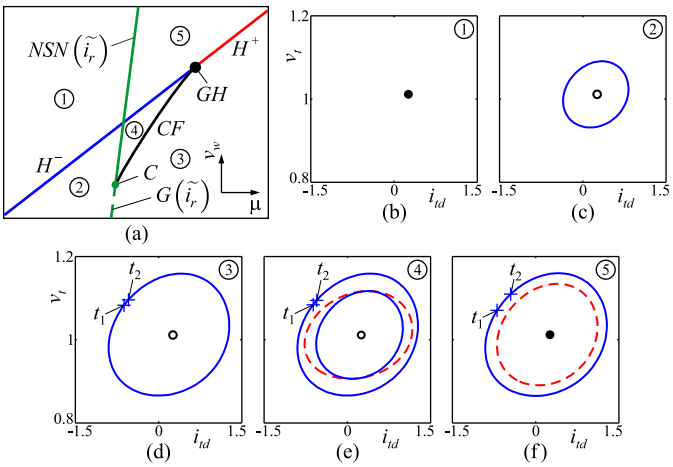

Fig. 8. Schematic diagram close to the generalized Hopf bifurcation (GH) in Fig. 7(a). The phase portraits of regions 1 to 5 are depicted in panels (b)–(f), respectively.

[7] The color of the curves corresponds to the ones used for the markers in Fig. 5.

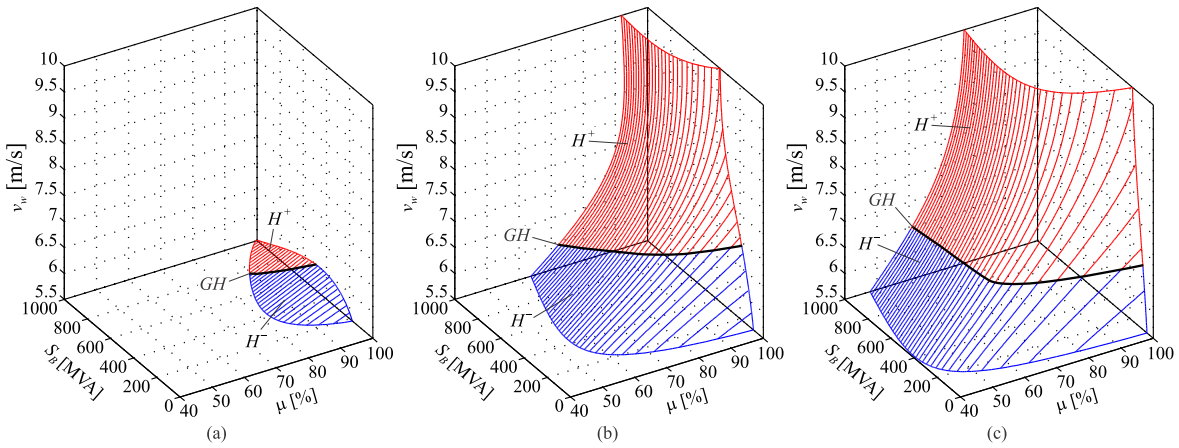

Fig. 9. Three-parameter bifurcation diagrams varying μ, S_B and v_w. (a) $K_{ir} = 0.015$. (b) $K_{ir} = 0.025$. (c) $K_{ir} = 0.035$. (For interpretation of the references to color in text near the reference citation, the reader is referred to the web version of this article.)

Fig. 8(d) indicate the switching instants t_1 and t_2 where the system crosses the boundary Σ_{12} (as those shown in Fig. 6(d), for $v_w = 6, 5$ m/s). The smooth cyclic fold bifurcation *CF*, creates a pair of cycles and thus in region 4 [Fig. 8(e)] there are three cycles, one unstable and two stable. The stable limit cycle created at *CF* in region 4 collapses with the equilibrium point, when crossing the curve H^- going from region 4 to region 5.[8] Then, in region 5 [Fig. 8(f)], the equilibrium point is stable and it is surrounded by an unstable cycle and a stable (non-smooth) cycle. Both cycles collapse and disappear at the non-smooth saddle-node curve $NSN(\widetilde{i_r})$ that separates region 5 from region 1.

The transition from the dynamics shown in the one-parameter diagrams of Fig. 5(b) and (c), is a consequence of the codimension-two singularities represented in Fig. 8(a). The proximity of the generalized Hopf bifurcation *GH* also explains the sharp form of the amplitude of the stable limit cycle in Fig. 5(b). Therefore, the structure depicted in Fig. 8(a) is the organizing center of the dynamics observed in the SSCI.

As noticed in Fig. 7(a), for wind speeds between 6 and 8.5 m/s, the limit cycle emerging at the Hopf bifurcation is affected mainly by grazing bifurcations due to the saturation of the rotor current (green curves). At low wind conditions, $v_w < 6$ m/s, the dynamics of the limit cycle is governed by the saturation of the GSC current. The curve associated to this saturation corresponds to grazing bifurcations that does not change the stability of the cycle [cf. orange dashed curve $G(\bar{i}_g)$]. The dynamics involved in the interaction between the grazing bifurcation curves $G(\widetilde{i_r})$ and $G(\bar{i}_g)$ includes other non-smooth phenomena that exist for larger compensation levels. For wind speeds $v_w > 8.5$ m/s, the dynamics of the emerging limit cycle involves additional phenomena as depicted in Fig. 5(d), and continued in the upper right corner in Fig. 7(a). In addition to the non-smooth saddle-node curve $NSN(\widetilde{i_r})$, the rotor voltage also introduces a non-smooth saddle-node curve $NSN(\widetilde{v_r})$, while the GSC current and the total current, two grazing bifurcation curves $G(\bar{i}_g)$ and $G(\widetilde{i_t})$, respectively. A smooth saddle-node bifurcation curve *CF* also arises in this parameter region.

It is important to notice that the non-smooth saddle-node curve, $NSN(\widetilde{i_r})$ in Fig. 7(a), remains very close to the Hopf curve. This is a positive fact for the system stability since the unstable limit cycle emerging from H^+ only exists in a vicinity of the Hopf curve and does not affect the operating region for lower compensation levels.

[8] It is also possible to reach region 3 from region 5 by crossing the subcritical Hopf curve H^+, collapsing the unstable limit cycle.

4.1.2. *Bifurcation diagram varying μ and S_B*

The two-parameter diagram is shown in Fig. 7(b). In this case the wind speed is fixed at 6.5 m/s. We can distinguish two different situations depending on the value of S_B. For $150 < S_B < 500$ MVA, the compensation level for which the Hopf bifurcation occurs, decreases for increasing values of S_B. Whereas for $S_B > 500$ MVA, the increase of S_B bends the Hopf bifurcation slightly towards the right, i.e., the bifurcation occurs for increasing values of μ. Therefore, for this wind speed the equilibrium point does not undergo a Hopf bifurcation if $\mu < 75\%$ for any value of S_B.

Notice that in this case the Hopf curve also suffers a generalized Hopf bifurcation (*GH*), and the structure shown in the blow-up of Fig. 7(b) has the same features than the one shown in Fig. 8.

4.2. *Three-parameter analysis*

In order to show the effects of the compensation level (μ), the rated power of the WF (S_B) and the wind speed (v_w) on the Hopf and the generalized Hopf bifurcations involved in the SSCI phenomenon, a three-parameter bifurcation diagram is performed. Fig. 9 depicts the results for different values of the gain of the inner RSC control loop used in the eigenvalue analysis of Fig. 4.

Here, the blue curves are supercritical Hopf bifurcations, the red ones are subcritical Hopf and the black ones are the curves of generalized Hopf bifurcations. The structure of bifurcation curves involved in the interaction of smooth and non-smooth bifurcations (point *C* in Fig. 8) can be found in a vicinity of the generalized Hopf curves in Fig. 9. Moreover, there is a surface of non-smooth saddle-node of limit cycles $NSN(\widetilde{i_r})$ that remains close to the subcritical part of the Hopf surfaces.

It is worth noticing that the actual variations of the operation point expected for a given WF (for example, due to variations in the wind speed) is a subset of the entire parameter space. In other words, given the nominal power of the WF (S_B), the series compensation level (μ) and the rotor gain (K_{ir}), the corresponding operating points will only depend on v_w, hence, they will define a vertical line in one of the bifurcation diagrams of Fig. 9. If such line intersects the Hopf surface, then the system will experience sustained SSO, if not, this methodology offers a measure of the distance to the instability by means of evaluating the proximity to the Hopf surface for all possible operating points of the WF. This figure of merit is valid for steady-state operation, nevertheless it is known that as the operating point gets closer to the bifurcation surface the system will become less robust to perturbations.

By comparing the three panels in Fig. 9, it is clear that the decrease (increase) in the gain K_{ir}, i.e., decreasing (increasing) the

bandwidth of the inner loop controller, brings the Hopf surface towards the right (left), enlarging (reducing) the stable region. Therefore, decreasing the bandwidth of the rotor current control loop reduces the risk of developing SSO. This and other modifications are analyzed in [4], nevertheless the authors also alert that the reduction of the rotor gain can deteriorate the transient response. Although the analysis of the mitigation technique is beyond the scope of this paper, the effect of K_{ir} on the Hopf surface suggests that modifications on the power converter control, can be made in order to damp the SSO. This is in concordance with the results presented in [4,6] for the ERCOT system (Texas) and in [18] for the Patagonia corridor (Argentina), where a supplementary controller is added to the RSC, that successfully damps the SSO with a small control action. Moreover, [15,16] propose other structures for the supplementary controller acting on the GSC, that also produce good results. An important feature of the mitigation strategies is the signal used as the control input. In this case, the typical choices are the rotor speed, the current through the line and the voltage across the series capacitor. In [13,19] it is shown that the voltage across the capacitor has the best characteristics, but it requires a remote measurement that introduces a time delay in the control loop. An alternative to this signal is proposed in [13,17] where the voltage across the capacitor is calculated integrating the line current. Other SSO countermeasure strategies use FACTS such as static var compensator, thyristor-controlled series capacitor, gate-controlled series capacitor or static synchronous compensator. An updated literature review of different mitigation techniques, including those using FACTS devices and modifications to the power converters controllers, can be found in [45].

5. Conclusions

This paper shows a multi-parameter analysis of the SSCI phenomenon using a combination of classical methods (e.g., eigenvalue analysis) and bifurcation theory. Key parameters, such as the wind speed, the compensation level, the WF rated power and the gain of the rotor current controllers, were varied in order to detect the onset of SSCI. The subsequent loss of the equilibrium point stability is due to a Hopf bifurcation, and depending on the parameter values, it can lead to a stable oscillation (when it is supercritical) or to an unstable one (when it is subcritical). The two-parameter analysis reveals that this change in the stability is explained by the presence of a generalized Hopf bifurcation. In addition, the sustained oscillation observed in practice can be originated either by the supercritical Hopf bifurcation or by grazing bifurcations of limit cycles, a non-smooth phenomenon introduced by saturations. When the Hopf bifurcation is supercritical, the grazing bifurcation does not change the stability but limits the amplitude of the limit cycle to a value practically constant. On the other hand, when the Hopf bifurcation is subcritical, the emerging unstable limit cycle vanishes (changing the stability) due to a non-smooth saddle-node generated by the grazing bifurcation. This prevents the unstable cycle from affecting the stable operating region. Thus, the grazing bifurcation of the reference current of the RSC plays an important role in the oscillation arising in SSCI.

The effects of decreasing the gain of the rotor current control loop (and its bandwidth), is clearly exposed by the displacement of the stability boundary (Hopf bifurcation curve) to the right in the corresponding three-parameter bifurcation diagrams, enlarging the stability region (allowing higher series compensation levels on the transmission line). The results obtained varying the rated power of the WF indicate that the wind energy penetration also restricts the feasible operating region. In other words, it is observed that the higher the power ratio between the equivalent grid and the wind generation, the higher the damping ratio of the subsynchronous mode. Finally, this kind of multi-parameter bifurcation analysis offers a methodology to analyze the dynamics related to SSI on a broad parameter set and can be used to determine the effectiveness of a mitigation strategy by comparing the resulting bifurcation diagrams with and without the supplementary controller. In other words, it provides an analysis tool to verify that the dynamics introduced by the new controller (often tuned for a determined operating condition), does not generate any negative effect on the system stability for a wide range of parameter values.

Acknowledgments

This work was supported by UNS (PGI 24/K064), ANPCyT (PICT 2014-2161) and CONICET (PIP 112-2012 01-00144).

Appendix A. State variables and system parameter values

The DFIG is represented by a fourth order model (zero sequence is neglected) with the stator currents i_{sd} and i_{sq}, and the rotor currents i_{rd} and i_{rq}, as dynamic states. A six-mass model is used to represent the mechanical system. The state variables are the angles of the blades, the hub, and the gearbox, with respect to the generator rotor (denoted as $\gamma_{1,\ldots,5}$, respectively), and the corresponding angular speeds of the masses ($\omega_{1,\ldots,6}$). The inertia and damping coefficients of the mechanical system are listed in Table A.1. The

Table A.1
System parameter values.

Description	Parameter	Value
DFIG (individual machine data)		
Rated power	S_N	2 MVA
Stator voltage/frequency	v_s/f_s	690 V/50 Hz
Number of poles	N_p	4
Gearbox constant	N_{gb}	129.6
Turbine radius	R_{tr}	46 m
Stator/rotor resistance	R_s/R_r	0.0108 pu/0.0121 pu
Stator/rotor self inductance	L_s/L_r	3.4640 pu/3.4720 pu
Mutual inductance	L_m	3.362 pu
GSC inductance	L_g	0.33 pu
dc-link capacitor	C_{dc}	10 mF
dc-link nominal voltage	v_{dc}	1200 V
Inertia const./damping coeff. blades	$H_{1,2,3}/D_{1,2,3}$	0.6388 s/0.004 s
Inertia const./damping coeff. hub	H_4/D_4	0.0114 s/0.010 pu
Inertia const./damping coeff. gearbox	H_5/D_5	0.0806 s/0.022 pu
Inertia const./damping coeff. rotor	H_6/D_6	0.1419 s/0.010 pu
Damping/stiffness coeff. blades-hub	D_{14}/K_{14}	4.8 pu/8.020 pu/rad
Damping/stiffness coeff. hub-gearbox	D_{45}/K_{45}	1.4 pu/0.349 pu/rad
Damping/stiffness coeff. gearbox-rotor	D_{56}/K_{46}	4.0 pu/11.67 pu/rad
Phase-locked loop		
PLL PI controller	K_{pll}/T_{pll}	87.96/0.022
DFIG RSC control (see Fig. 2)		
Voltage droop constant	k_v	0.05
Terminal voltage PI	K_{vt}/T_{ivt}	13.5/3.6
MPPT algorithm		see [35, Section III]
External loops PI	K_{er}/T_{ier}	0.5/0.075
Internal loops PI	K_{ir}/T_{iir}	0.025/0.0675
RSC limits	$\bar{i}_t/\bar{i}_r/\bar{v}_r$	1.0/0.33/1.15
DFIG GSC control (see Fig. 2)		
dc-link PI controller	K_{vdc}/T_{ivdc}	0.35/0.2
GSC PI controllers	K_g/T_{ig}	1/0.01
GSC limits	$\bar{i}_g/\bar{v}_g$	0.33/1.15
Electric network (bases: 100 MVA, 500 kV)		
Transmission line length	l_{line}	354 km
Transmission line resistance/inductance	R_{line}/L_{line}	0.00275 pu/0.03384 pu
WF internal grid (gen. capacity: 500 MVA)	R_{wf}/R_{wf}	0.00206 pu/0.03885 pu
Equivalent grid short-circuit power	S_{eq}	7000 MVA

Table A.2
Power flows of a 500 MVA WF operating at four different wind speeds (μ = 50%).

Description	5.5 m/s	6.5 m/s	8 m/s	10 m/s
Equivalent grid voltage	1.0∠0°	1.0∠0°	1.0∠0°	1.0∠0°
Terminal voltage	1.01∠2.88°	1.01∠4.81°	1.01∠9.01°	1.008∠17.75°
WF active power [MW]	73.64	121.74	226.94	442.32
WF reactive power [MVAr]	−3.24	−4.52	−2.39	23.6

power converters of the DFIG are represented by their corresponding averaged models with the vector control schemes depicted in Fig. 2. In particular, the RSC control has four state equations associated to the PI controllers, plus two states corresponding to a phase-locked loop (PLL), and one more belonging to the terminal voltage controller (internal PI state). On the other hand, six dynamic equations are used for the GSC: two for the GSC current i_{gd} and i_{gq}, two for the internal states of the PI controllers, and two for the dc-link. The electric network is modeled by six dynamic equations representing the terminal voltage v_{td} and v_{tq}, the line current i_{ld} and i_{lq}, and the voltage across the series capacitor v_{cd} and v_{cq}. The parameters of the transmission line are summarized in Table A.1. The resulting model has 34 state equations.

Table A.2 shows the power flows of a 500 MVA WF operating at four different wind speeds (v_w = 5.5, 6.5, 8 and 10 m/s).

References

[1] ABB Technical Publication, Fixed Series Compensation, 2016, URL http://new.abb.com/facts/fixed-series-compensation.
[2] ABB Technical Publication, Series Compensation: Boosting Transmission Capacity, 2010, pp. 1–16, URL www.abb.com/FACTS.
[3] L. Gross, Sub-synchronous grid conditions: new event, new problem, and new solutions, in: 37th Annual Western Protective Relay Conference, Spokane, Washington, USA, 2010, pp. 1–19.
[4] G. Irwin, A. Jindal, A. Isaacs, Sub-synchronous control interactions between type 3 wind turbines and series compensated AC transmission systems, in: IEEE Power and Energy Society General Meeting, San Diego, USA, 2011, pp. 1–6.
[5] G. Irwin, A. Isaacs, D. Woodford, Simulation requirements for analysis and mitigation of SSCI phenomena in wind farms, in: Transmission and Distribution Conference and Exposition, 2012 IEEE PES, Orlando, USA, 2012, pp. 1–4.
[6] A.E. Leon, J.A. Solsona, Sub-synchronous interaction damping control for DFIG wind turbines, IEEE Trans. Power Syst. 30 (1) (2015) 419–428.
[7] NERC, Lesson Learned. Sub-synchronous Interaction between Series-compensated Transmission Lines and Generation, Tech. Rep. 20110705, NERC, Atlanta, USA, 2011 July.
[8] L. Fan, R. Kavasseri, Z.L. Miao, C. Zhu, Modeling of DFIG-based wind farms for SSR analysis, IEEE Trans. Power Del. 25 (4) (2010) 2073–2082.
[9] L. Fan, C. Zhu, Z. Miao, M. Hu, Modal analysis of a DFIG-based wind farm interfaced with a series compensated network, IEEE Trans. Energy Convers. 26 (4) (2011) 1010–1020.
[10] Z. Miao, Impedance-model-based SSR analysis for type 3 wind generator and series-compensated network, IEEE Trans. Energy Convers. 27 (4) (2012) 984–991.
[11] D. Suriyaarachchi, U. Annakkage, C. Karawita, D. Jacobson, A procedure to study sub-synchronous interactions in wind integrated power systems, IEEE Trans. Power Syst. 28 (1) (2013) 377–384.
[12] B. Badrzadeh, M. Sahni, Y. Zhou, D. Muthumuni, A. Gole, General methodology for analysis of sub-synchronous interaction in wind power plants, IEEE Trans. Power Syst. 28 (2) (2013) 1858–1869.
[13] L. Fan, Z. Miao, Mitigating SSR using DFIG-based wind generation, IEEE Trans. Sustain. Energy 3 (3) (2012) 349–358.
[14] H. Mohammadpour, E. Santi, SSR damping controller design and optimal placement in rotor-side and grid-side converters of series-compensated DFIG-based wind farm, IEEE Trans. Sustain. Energy 6 (2) (2015) 388–399.
[15] H.A. Mohammadpour, A. Ghaderi, H. Mohammadpour, E. Santi, SSR damping in wind farms using observed-state feedback control of DFIG converters, Electr. Power Syst. Res. 123 (2015) 57–66.
[16] H. Mohammadpour, E. Santi, Optimal adaptive sub-synchronous resonance damping controller for a series-compensated doubly-fed induction generator-based wind farm, IET Renew. Power Gener. 9 (6) (2015) 669–681.
[17] P.-H. Huang, M. El Moursi, W. Xiao, J. Kirtley, Subsynchronous resonance mitigation for series-compensated DFIG-based wind farm by using two-degree-of-freedom control strategy, IEEE Trans. Power Syst. 30 (3) (2015) 1442–1454.
[18] A.E. Leon, Integration of DFIG-based wind farms into series-compensated transmission systems, IEEE Trans. Sustain. Energy 7 (2) (2016) 451–460.
[19] H. Mohammadpour, A. Ghaderi, E. Santi, Analysis of sub-synchronous resonance in doubly-fed induction generator-based wind farms interfaced with gate-controlled series capacitor, IET Gener. Transm. Distrib. 8 (12) (2014) 1998–2011.
[20] L. Piyasinghe, Z. Miao, J. Khazaei, L. Fan, Impedance model-based SSR analysis for TCSC compensated type-3 wind energy delivery systems, IEEE Trans. Sustain. Energy 6 (1) (2015) 179–187.
[21] H. Mohammadpour, E. Santi, Modeling and control of gate-controlled series capacitor interfaced with a DFIG-based wind farm, IEEE Trans. Ind. Electron. 62 (2) (2015) 1022–1033.
[22] K. Narendra, D. Fedirchuk, R. Midence, N. Zhang, A. Mulawarman, P. Mysore, V. Sood, New microprocessor based relay to monitor and protect power systems against sub-harmonics, in: 2011 IEEE Electrical Power and Energy Conference (EPEC), 2011, pp. 438–443.
[23] L. Wang, X. Xie, Q. Jiang, H. Liu, Y. Li, H. Liu, Investigation of SSR in practical DFIG-based wind farms connected to a series-compensated power system, IEEE Trans. Power Syst. 30 (5) (2015) 2772–2779.
[24] L. Wang, X. Xie, Q. Jiang, X. Liu, Centralised solution for subsynchronous control interaction of doubly fed induction generators using voltage-sourced converter, IET Gener. Transm. Distrib. 9 (16) (2015) 2751–2759.
[25] K.N. Srivastava, S.N. Singh, S.C. Srivastava, Effect of multiple equilibria on power system stability, Electr. Power Syst. Res. 55 (3) (2000) 165–172.
[26] W. Gu, F. Milano, P. Jiang, G. Tang, Hopf bifurcations induced by SVC controllers: a didactic example, Electr. Power Syst. Res. 77 (3–4) (2007) 234–240.
[27] F. Echavarren, E. Lobato, L. Rouco, Steady-state analysis of the effect of reactive generation limits in voltage stability, Electr. Power Syst. Res. 79 (9) (2009) 1292–1299.
[28] G. Revel, A.E. Leon, D.M. Alonso, J.L. Moiola, Bifurcation analysis on a multimachine power system model, IEEE Trans. Circuits Syst. I Fundam. Theory Appl. 57 (4) (2010) 937–949.
[29] J.E. Tobón, J.M. Ramirez, R.E.C. Gutierrez, Tracking the maximum power transfer and loadability limit from sensitivities-based impedance matching, Electr. Power Syst. Res. 119 (2015) 355–363.
[30] M. Perninge, Approximating the parameter-space stability boundary considering post-contingency corrective controls, Electr. Power Syst. Res. 121 (2015) 313–324.
[31] H.A. Pulgar-Painemal, R.I. Gálvez-Cubillos, Limit-induced bifurcation by wind farm voltage supervisory control, Electr. Power Syst. Res. 103 (2013) 122–128.
[32] G. Revel, A.E. Leon, D.M. Alonso, J.L. Moiola, Dynamics and stability analysis of a power system with a PMSG-based wind farm performing ancillary services, IEEE Trans. Circuits Syst. I Fundam. Theory Appl. 61 (7) (2014) 2182–2193.
[33] A.H. Nayfeh, A. Harb, C.-M. Chin, A.M. Hamdan, L. Mili, A bifurcation analysis of subsynchronous oscillations in power systems, Electr. Power Syst. Res. 47 (1) (1998) 21–28.
[34] M. Varghese, F. Wu, P. Varaiya, Bifurcations associated with sub-synchronous resonance, IEEE Trans. Power Syst. 13 (1) (1998) 139–144.
[35] J. Slootweg, S. de Haan, H. Polinder, W. Kling, General model for representing variable speed wind turbines in power system dynamics simulations, IEEE Trans. Power Syst. 18 (1) (2003) 144–151.
[36] R. Pena, J. Clare, G. Asher, Doubly fed induction generator using back-to-back PWM converters and its application to variable-speed wind-energy generation, IEE Proc. Electr. Power Appl. 143 (3) (1996) 231–241.
[37] A. Tapia, G. Tapia, J.X. Ostolaza, J.R. Sáenz, Modeling and control of a wind turbine driven doubly fed induction generator, IEEE Trans. Energy Convers. 8 (2) (2003) 194–204.
[38] K.J. Astrom, T. Hagglund, Advanced PID Control, ISA – Instrumentation, Systems, and Automation Society, Research Triangle Park, NC 27709, 2005.
[39] K. Clark, N.W. Miller, J.J. Sanchez-Gasca, Modeling of GE Wind Turbine-generators for Grid Studies, Version 4.5, Tech. Rep., General Electric International, Inc., 2010 April.
[40] A. Dhooge, W. Govaerts, Y.A. Kuznetsov, H.G.E. Meijer, B. Sautois, New features of the software MatCont for bifurcation analysis of dynamical systems, Math. Comput. Model Dyn. Syst. 14 (2) (2008) 147–175.
[41] Y.A. Kuznetsov, Elements of Applied Bifurcation Theory, 3rd ed., Springer-Verlag, New York, 2004.
[42] I.A. Hiskens, P.B. Reddy, Switching-induced stable limit cycles, Nonlinear Dyn. 50 (2007) 575–585.
[43] M. di Bernardo, C. Budd, A. Champneys, P. Kowalczyk, Piecewise-smooth Dynamical Systems. Theory and Applications, Springer-Verlag, London, 2008.
[44] V. Avrutin, E. Fossas, A. Granados, M. Schanz, Virtual orbits and two-parameter bifurcation analysis in a ZAD-controlled buck converter, Nonlinear Dyn. 63 (1–2) (2011) 19–33.
[45] V. Virulkar, G. Gotmare, Sub-synchronous resonance in series compensated wind farm: a review, Renew. Sustain. Energy Rev. 55 (2016) 1010–1029.